

Patterning enhanced tetragonality in BiFeO₃ thin films with effective negative pressure by helium implantation

C. Toulouse^{1,2,*}, J. Fischer³, S. Farokhipoor⁴, L. Yedra⁵, F. Carlà^{6,7}, A. Jarnac⁸, E. Elkaim⁸, P. Fertey⁸, J.-N. Audinot², T. Wirtz², B. Noheda⁴, V. Garcia³, S. Fusil³, I. Peral Alonso¹, M. Guennou¹, and J. Kreisel¹

¹Department of Physics and Materials Science, University of Luxembourg, 41 rue du Brill, L-4422 Belvaux, Luxembourg

²Materials Research and Technology Department,

Luxembourg Institute of Science and Technology, 41 rue du Brill, L-4422 Belvaux, Luxembourg

³Unité Mixte de Physique, CNRS, Thales, Université Paris-Saclay, F-91767 Palaiseau, France

⁴Zernike Institute for Advanced Materials, University of Groningen, Nijenborgh 4, NL-9747AG Groningen, The Netherlands

⁵Laboratoire Structures, Propriétés et Modélisation des Solides (UMR CNRS 8580) and Laboratoire Mécanique des Sols, Structures et Matériaux (UMR CNRS 8579), CentraleSupélec, Université Paris Saclay, F-91192 Gif-sur-Yvette Cedex, France

⁶European Synchrotron Radiation Facility, 71 Avenue des Martyrs, F-38000 Grenoble, France

⁷Diamond Light Source Ltd., Didcot OX11 0DE, United Kingdom

⁸Synchrotron SOLEIL, L'Orme des Merisiers, F-91190 Saint-Aubin, Gif-sur-Yvette, France



(Received 22 September 2020; accepted 11 January 2021; published 9 February 2021)

Helium implantation in epitaxial thin films is a way to control the out-of-plane deformation independently from the in-plane strain controlled by epitaxy. In particular, implantation by means of a helium microscope allows for local implantation and patterning down to the nanometer resolution, which is of interest for device applications. We present here a study of bismuth ferrite (BiFeO₃) films where strain was patterned locally by helium implantation. Our combined Raman, x-ray diffraction, and transmission electron microscopy (TEM) study shows that the implantation causes an elongation of the BiFeO₃ unit cell and ultimately a transition towards the so-called supertetragonal polymorph via states with mixed phases. In addition, TEM reveals the onset of amorphization at a threshold dose that does not seem to impede the overall increase in tetragonality. The phase transition from the R-like to T-like BiFeO₃ appears as first-order in character, with regions of phase coexistence and abrupt changes in lattice parameters.

DOI: [10.1103/PhysRevMaterials.5.024404](https://doi.org/10.1103/PhysRevMaterials.5.024404)

I. INTRODUCTION

Strain engineering has arisen in the last decade as an essential means to tune physical properties in functional thin films. The most common way to tune strain in films is by using epitaxial strain, imposing an in-plane biaxial strain to the material due to the lattice misfit with the substrate on which the film is grown. The strain state can be varied by using different substrates, or even in some instances can be tuned continuously, for example, by an electric field applied on a piezoelectric substrate [1–3]. Using this approach, it has been demonstrated that the properties of the films can be controlled and modified, sometimes spectacularly. Remarkable results have included induced ferroelectricity [4–7], a modified magnetic ground state of multiferroic compounds [8–10] or strain-induced structural transitions [11–14]. In this classical approach of strain engineering, only the in-plane biaxial strain is controlled; the out-of-plane strain is fixed by the elastic equilibrium of the system but cannot be controlled independently.

Controlling this additional strain parameter, and in particular achieving an elongation of the unit cell (“negative pressure”), is of high interest. Negative pressure has, indeed, been theoretically predicted to trigger various properties modifications [15–18]. Experimentally, it can be achieved by helium implantation. Due to its nobility, helium implants interstitially, without chemical substitution, thus inducing a “swelling” of the host material’s unit cell volume [19]. Helium implantation is customarily achieved by laboratory ion sources [7,20–23], similar to those used for wafer processing in semiconductor engineering. Another route—the one chosen in the present work—is to use a helium ion microscope as a way to implant ions locally. This technique has recently started to be used as a means of defect engineering [24,25], but our study is aiming at using a helium microscope for strain-engineering purposes. The interest of this method lies in particular in the nanopatterning possibilities allowed by the sub-nanometer resolution of the microscope [26]. Moreover, it has been demonstrated recently that helium implantation is a reversible process and that the helium trapped can be released with annealing at high temperatures above 650 °C and under oxygen atmosphere [20], allowing for reversible properties tuning. For instance, a very recent study on FeRh thin films shows that local helium implantation allows for direct writing of nanoscale domains with a metamagnetic order tunable with

*Present address: Department of Physics and Materials Science, University of Luxembourg, LIST-Belvaux site, 41 rue du Brill, L-4422 Belvaux, Luxembourg; Corresponding author: constance.toulouse@uni.lu

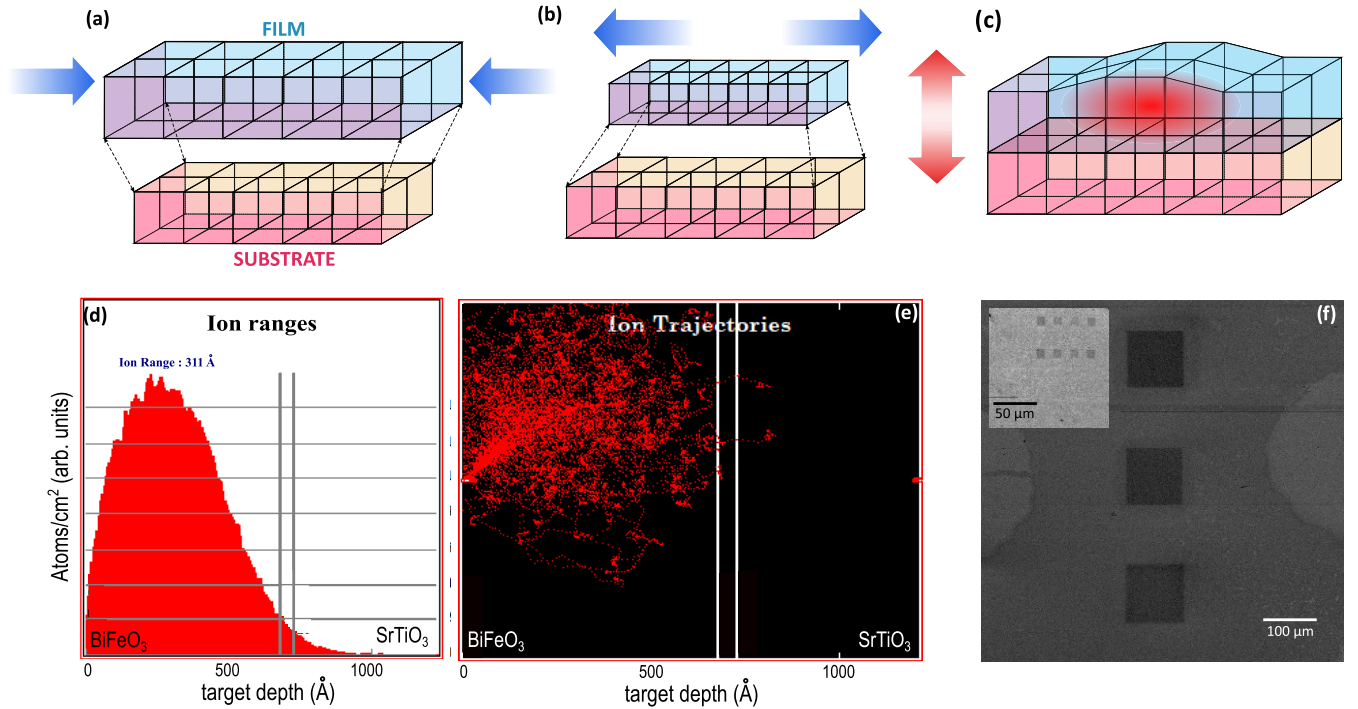


FIG. 1. Schematic representations of (a) compressive and (b) tensile epitaxial strain and of (c) the out-of-plane negative pressure induced by helium implantation. TRIM simulations (see “Experimental details” section for details) of (d) the helium-ion distribution and (e) the implantation depth profile of 6 keV helium ions inside BiFeO₃(70 nm)/SrRuO₃(5 nm)/SrTiO₃ with an incident angle of 49°. (f) Secondary electron images (SEM-HIM) of patterned BiFeO₃ films with various sizes of implanted regions.

the implanted dose, demonstrating the application potential of this technique [27].

Here we demonstrate the use of a helium ion microscope to perform strain engineering by helium implantation on bismuth ferrite (BiFeO₃) thin films. BiFeO₃ is one of the most studied multiferroic compounds, as it exhibits multiferroicity well above room temperature. In its bulk form it develops below $T_C = 1143$ K a very large ferroelectric polarization [28] ($P = 100 \mu\text{C cm}^{-2}$) along the [111] direction of its pseudocubic structure and exhibits below $T_N = 643$ K a G-type antiferromagnetic ordering of the iron spins with a superimposed long-range cycloidal modulation in a plane containing the ferroelectric local mode vector [29]. In its thin-film form, BiFeO₃ undergoes a structural transition under epitaxial strain. At low strain, it crystallizes in a so-called R phase in, a monoclinic M_A structure with only a slight distortion from the bulk $R3c$ rhombohedral structure. At high strain or under certain growth conditions, BiFeO₃ can exhibit a phase with enhanced tetragonality (with a c/a ratio between 1.22 and 1.25) in the monoclinic M_C structure called the supertetragonal or T phase in which an enhanced ferroelectric polarization has been observed and theoretically reproduced [30]. Many studies report the existence of intermediate mixed R-T phases in BiFeO₃ films, with a 3° tilt of the monoclinic angle between the phases [31]. Regarding functional properties, epitaxial strain has been shown to modify the ferroic properties of BiFeO₃ films: the ferroelectric Curie transition temperature is decreased under epitaxial strain [32] while the bulklike magnetic cycloid present at low strain is destroyed at high epitaxial strain, both tensile and compressive, giving place to a canted antiferromagnetic state [9,10].

By combining epitaxial strain and helium implantation, a full tridimensional control of strain in thin films can be achieved. The lattice misfit between the substrate and the film’s native bulk compound causes a biaxial strain in the plane of epitaxy [Figs. 1(a) and 1(b)]. Due to the in-plane clamping of the film to its substrate, helium implantation gives rise to an out-of-plane negative pressure, without modification in plane [Fig. 1(c)]. In the case of BiFeO₃ thin films, helium implantation allows one to trigger the transition towards the supertetragonal phase by enhancing tetragonality due to this out-of-plane strain tuning. It has been shown recently that large-scale helium implantation on epitaxial BiFeO₃ films can induce the supertetragonal phase on the LSAT substrate while enhancing tetragonality in R-like and T-like films grown on SrTiO₃ and LaAlO₃, respectively [23]. This raises important questions regarding the transition from the R-like to T-like structure, here caused by continuously varying the helium dose: character of the transition, possibility of coexistence between the two phases, presence of interfaces, etc. Here, by combining local and nonlocal probes, we bring insight to the mechanism of this R-to-T structural transition under helium implantation, which appears first order in character. In addition, we show that local helium implantation allows one to pattern the tetragonality of the structure while preserving crystal quality, demonstrating the possibility to structurally pattern BiFeO₃ films.

II. EXPERIMENTAL DETAILS

BiFeO₃ epitaxial films were grown by pulsed laser deposition on (001)-oriented SrTiO₃ (−1.5% lattice misfit with

BiFeO₃) and DyScO₃ (−0.4% lattice misfit) substrates with a 5-nm-thick SrRuO₃ bottom electrode as described in Refs. [33–35]. The thickness of the films was set to 60 nm. For the film grown on DyScO₃, this is thin enough to avoid strain relaxation, while for the film grown on SrTiO₃, the formation of in-plane ferroelastic 71° domains induce partial strain relaxation already at 60-nm thickness, but their alternation allows for overall epitaxial matching with the substrate [36].

Helium implantation of our films was performed using an Orion NanoFab helium ion microscope (HIM) [37]. Various doses of 6-keV helium ions were implanted into square regions with sizes ranging from 10 × 10 to 500 × 500 μm² [Fig. 1(f)]. We kept the doses below 1 × 10¹⁶ ions cm^{−2}, which, at the energy used, is below the threshold for structural defect formation [38–40]. The implantation parameters, in particular the beam energy and the impact angle, were determined by SRIM [41] (stopping range of ions in matter) and TRIM (transport of ions in matter) simulations in order to have the maximum of the implantation profile inside the film [Figs. 1(d) and 1(e)]. The samples were therefore tilted 49° from normal to reduce helium implantation in the bottom electrode and the substrate while also avoiding channeling through the crystal structure's easy planes. The TRIM simulations of the implanted ion distribution and depth profile—taking density values of 8.408 g cm^{−3} for BiFeO₃, 6.49 g cm^{−3} for SrRuO₃, and of 5.11 g cm^{−3} for SrTiO₃ as taken from the literature [42,43]—are shown in Figs. 1(d) and 1(e).

To probe our implanted samples, we used Raman spectroscopy, electron microscopy, and x-ray diffraction (XRD) techniques. Micro-Raman measurements were performed with a 442-nm He-Cd laser in an inVia Renishaw micro-Raman spectrometer. Depth profiles were acquired by varying the focus, meaning the distance between the objective and the sample, with 0.2 μm steps. Principle components analysis (PCA) and non-negative matrix factorization (NMF), using the R-DATA software as described in Ref. [44], allow extraction of the layer's signal from the overall substrate's contribution.

Transmission electron microscopy (TEM) studies of cross-sectional samples were performed in a probe corrected FEI Titan³ G2 60-300 working at 300 kV in scanning mode (STEM) using a high-angle annular dark-field detector (HAADF). The microscope is equipped with a Bruker Super-X energy-dispersive x-ray spectroscope (EDX), used for obtaining elemental maps. Geometrical phase analysis (GPA) [45] using STRAIN++ software, was applied on atomically resolved HAADF images in order to measure local deformations of the lattice.

The XRD synchrotron data were collected at two different synchrotron sources. Diffracted intensity maps were recorded at the ID03 surface diffraction beamline of the ESRF using the six-circle vertical diffractometer. The experiment was conducted using an incident wavelength of 0.516 Å (24 keV) and a beam size of 43 × 28 μm² (horizontal × vertical). For the grazing-incidence experiments, an incidence angle of 3 deg was used and allowed us to produce a beam footprint on the sample surface with a size comparable to the area of the implanted region. The implanted region was aligned in the beam using a camera with a macrolense and the visible fluorescence of the sample under the x-ray beam irradiation. The data were collected using a Maxipix pixel detector and

processed using the BINoculars code. At the CRISTAL Beamline of SOLEIL Synchrotron, we performed localized XRD measurements on a six-circle diffractometer using a beam size of 30 × 100 μm², with an imXpad pixel detector and a wavelength of 1.2471 Å. The implanted regions could be localized easily, due to their different 00/ XRD signal, by scanning the sample spatially. All the diffraction data are reported using the substrate lattices as reference systems.

III. RESULTS AND DISCUSSION

A. Raman spectroscopy

Raman spectroscopy measurements were performed to study the effect of implantation on the lattice via the phonon modes. Thin films make it naturally increasingly difficult to single out the signal of the film from the substrate contribution. However, due to the broad peaks of Raman signal of SrTiO₃, some sharper Raman modes from the BiFeO₃ layer were observable in our BiFeO₃/SrTiO₃ sample. Raman spectra measured on regions with different doses are shown in Fig. 2(a). Two low-energy phonon modes can be seen emerging from the substrate's signal at 146 and 184 cm^{−1}. These phonon modes correspond to Raman excitations with A₁(LO) symmetry, usually measured around 145–147 and 176–180 cm^{−1}, respectively [46,47].

Furthermore, we performed Raman depth profiles by continuously varying the distance between the sample and the Raman objective, following the approach described in Ref. [44]. Figures 2(b) and Fig. 2(c) present the principal component analysis (PCA) of the Raman signal obtained on the nonimplanted part of the film. Figure 2(b) shows the signal associated to the first two components, while Fig. 2(c) shows their intensity profile as a function of depth. The first component of the PCA visibly corresponds to the SrTiO₃ signal: it has the same shape as the well-known SrTiO₃ second-order Raman signal [Fig. 2(b), top], while its intensity continuously increases when the distance between the sample and the objective decreases [Fig. 2(c), top]. This is in agreement with the signal coming from the substrate, further away from the objective. The second component of the PCA presents a signal where three narrow peaks can be observed at 146, 184, and 226 cm^{−1} [Fig. 2(b), bottom]. These peaks corresponds to the two BiFeO₃ Raman modes observed in the spectra of Fig. 2(a), with an additional peak at 226 cm^{−1} also associated to an A₁(LO) Raman mode of BiFeO₃ in the literature [46,47]. The intensity depth profile of this second component presents a maximum in the depth range corresponding to the film [Fig. 2(c), bottom], which confirms that we can indeed attribute it to the Raman signal of the BiFeO₃ film.

By comparing the evolution of the Raman signal with the implanted helium dose, we observe that the Raman signal of the BiFeO₃ film disappears with increasing dose while not shifting in frequency. Indeed, the two phonon modes are visible only for the virgin film and the lowest dose [5 × 10¹⁴ He cm^{−2}, Fig. 2(a)]. The Raman spectrum of BiFeO₃ could not be seen for the films deposited on the DyScO₃ substrate due to a stronger substrate contribution.

Several causes can be envisioned to explain the disappearance of the Raman signal. In the context of BiFeO₃ in

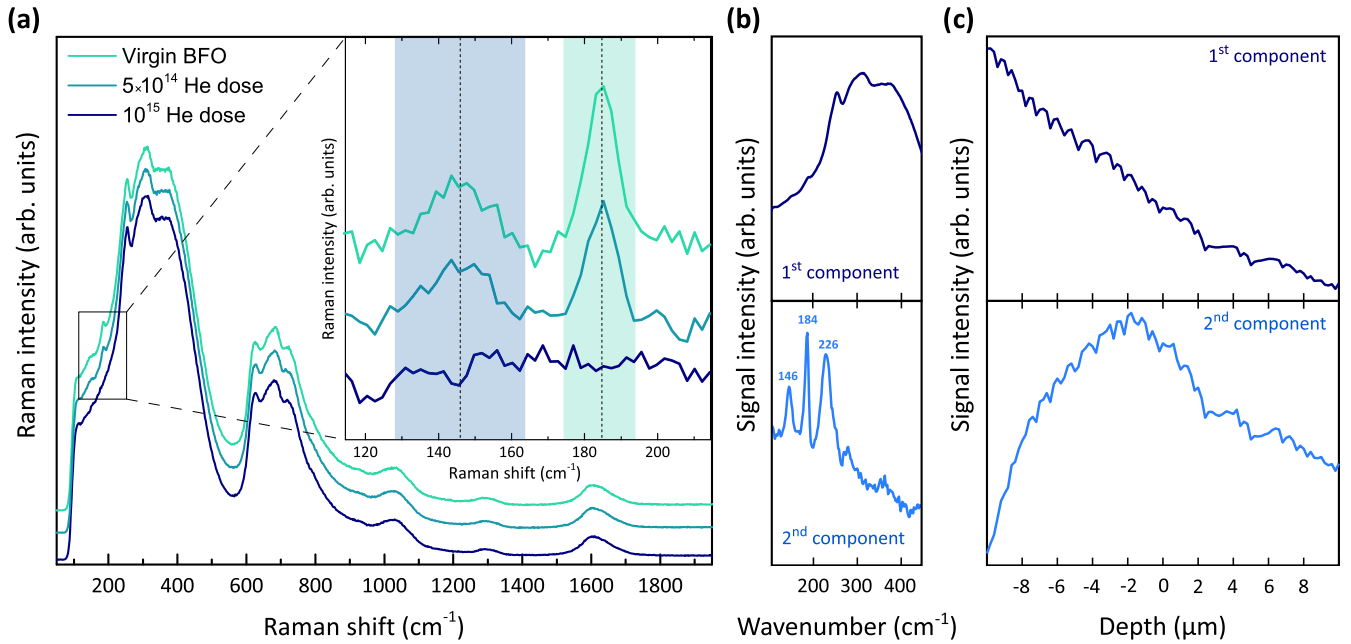


FIG. 2. (a) Raman spectra performed on different regions of the $\text{BiFeO}_3/\text{SrTiO}_3$ film. The underlying intense signal of SrTiO_3 is dominant, but some BiFeO_3 phonon modes can be singled out. The inset shows these phonon modes, with a baseline subtraction. The colored regions and dotted lines are guides for the viewer. [(b),(c)] Principal component analysis of the depth profiles on a nonimplanted region of the film: we can see the component signal (b) and the associated depth profiles (c) for the first two components associated to the substrate and the film, respectively.

particular, the Raman signal of the supertetragonal phase is weaker by one order of magnitude than the signal for the rhombohedral-like structure [48]. The disappearance of the Raman signal under implantation can therefore be a signature of a transition towards an increased tetragonality, as we would expect (cf. Fig. 1(c) and Ref. [23]). Alternatively, a vanishing Raman spectrum can be associated to a transition towards a metallic character, which in BiFeO_3 is known to happen at very high temperatures and pressure. In this particular context, it is also conceivable that an increase in band gap—i.e., a decrease in absorption—would lead to a decrease in intensity of the Raman spectrum as compared to the substrate. Finally, we cannot exclude an effect directly due to the presence of He in the BiFeO_3 lattice, decreasing the Raman intensity.

B. Transmission electron microscopy

To gain more insight into the effect of implantation at the local scale, transmission electron microscopy was performed on samples from a BiFeO_3 layer grown on a SrTiO_3 (001) substrate, with doses 5×10^{15} and 1×10^{16} He cm^{-2} .

The HAADF STEM images of the $\text{BiFeO}_3/\text{SrTiO}_3$ interfaces in the two implanted regions are shown in Figs. 3(a) and 3(b). No amorphization of the BiFeO_3 layer is visible for the 5×10^{15} He cm^{-2} dose region: the epitaxial columns are clearly visible throughout the film although some structural defects are present (as expected under implantation). When the implanted dose is increased to a higher level, however, some regions of amorphization are observed [Fig. 3(b)]. Their characteristic size is of the order of the nanometer and is reminiscent of the observation of defect “nanobubbles” previously reported upon He implantation on silicon [38].

To gain insight into the strain induced locally by helium implantation, GPA was performed on samples prepared with 5×10^{15} and 1×10^{16} He cm^{-2} doses, taking the SrTiO_3 lattice as a reference. We see in Figs. 3(c) and 3(e) the in-plane strain for both doses, while the out-of-plane strain is shown on Figs. 3(d) and 3(f). While it is apparent from the GPA strain maps that local deformations in plane are very small, we observe stronger out-of-plane deformations, consistent with an out-of-plane swelling induced by implantation. The strain seems to increase with the dose between Figs. 3(d) and 3(f), as expected for an enhanced tetragonality.

Furthermore, we extracted the average lattice parameters by performing Fourier transform of the STEM images in the two regions with 5×10^{15} and 1×10^{16} He cm^{-2} doses as well as in a pristine nonimplanted region as a reference. They are given in Table I. Each lattice parameter was estimated from ten images, and the error bars arise from the standard deviation of the measurements. We can clearly see that the in-plane lattice parameter remains unchanged, while a c -lattice expansion, increasing with the helium dose, is observed with implantation. Moreover, we can observe that in the region implanted with the highest dose, the c -axis lattice parameter extracted by Fourier transform has a much broader error bar, consistent with a loss of crystallinity of the film, as visible from Fig. 3(b).

Finally, EDX chemical analysis of the atoms at the interface between the substrate and the film (with the 5-nm-thick SrRuO_3 bottom electrode) was performed and is presented in Fig. 3(g). The chemical compositions of the substrate, the bottom electrode, and the layer are well resolved and the compositional interfaces correspond to those of the HAADF image, with no indication of chemical intermixing.

TABLE I. Lattice parameters extracted from the STEM measurements. The discrepancy between the usual SrTiO_3 cubic lattice parameter of 3.905 \AA and the extracted ones in the a direction comes from the calibration of the microscope combined with sample drift. We chose to keep the values as extracted from the images, the values in the c axis being in agreement with literature. The last column shows the c/a ratio, calculated with the a lattice parameter of SrTiO_3 from literature: $a_{\text{STO}} = 3.905 \text{ \AA}$.

Sample	a	c	c/a_{STO}
STO substrate	$3.79 \pm 0.02 \text{ \AA}$	$3.92 \pm 0.03 \text{ \AA}$	
BFO pristine	$3.82 \pm 0.02 \text{ \AA}$	$4.02 \pm 0.02 \text{ \AA}$	1.03
BFO ($5 \times 10^{15} \text{ He cm}^{-2}$)	$3.79 \pm 0.01 \text{ \AA}$	$4.38 \pm 0.05 \text{ \AA}$	1.12
BFO ($1 \times 10^{16} \text{ He cm}^{-2}$)	$3.78 \pm 0.04 \text{ \AA}$	$4.57 \pm 0.10 \text{ \AA}$	1.17

Furthermore, no migration of the atoms of the layer to the bottom electrode or substrate is observed under implantation.

C. Synchrotron XRD

To determine the effect of helium implantation on the structure of our BiFeO_3 layers, we performed micro-XRD using specular reflectivity and grazing-incidence geometry. Figure 4(a) shows the specular reflectivity curve measured

inside an implanted region (with $5 \times 10^{15} \text{ He cm}^{-2}$ dose) on a BiFeO_3 film grown on SrTiO_3 substrate. It shows, in addition to the (001) Bragg peaks of the SrTiO_3 substrate and the BiFeO_3 layer, a new phase with a c -lattice expansion, revealed by the new peak appearing at $l = 0.89 \text{ r.l.u}$ [Fig. 4(a)].

From the in-plane diffracted intensity maps measured at different l values it was possible to verify that all the phases have the same in-plane lattice parameters of the substrate, as observed locally from the TEM results. A comparison between the hk maps collected at $l = 0.96$ for the implanted and nonimplanted regions [Fig. 4(b)] shows no difference in the positions of the BiFeO_3 Bragg peaks, indicating no modification of the in-plane lattice parameter as a consequence of the implantation process: as expected, the clamping to the substrate locks the film parameters in the epitaxial plane. Figure 4(c) shows the hl maps around the (001) Bragg peak of the SrTiO_3 substrate outside and inside an implanted region (with $5 \times 10^{15} \text{ He cm}^{-2}$ dose). The (001) peak of the substrate and, at lower l , of the BiFeO_3 layer, are clearly visible while a new phase, with a c -lattice expansion of 7.9% (from 4.072 to 4.395 \AA), is observed in the implanted region, consistent with the values extracted from the TEM images. Figure 4(d) shows a closeup of the $(10l)$ rod around the (001) region in which the coexistence of the new structural phase and the pristine BiFeO_3 layer are visible. This can be explained by a mixing

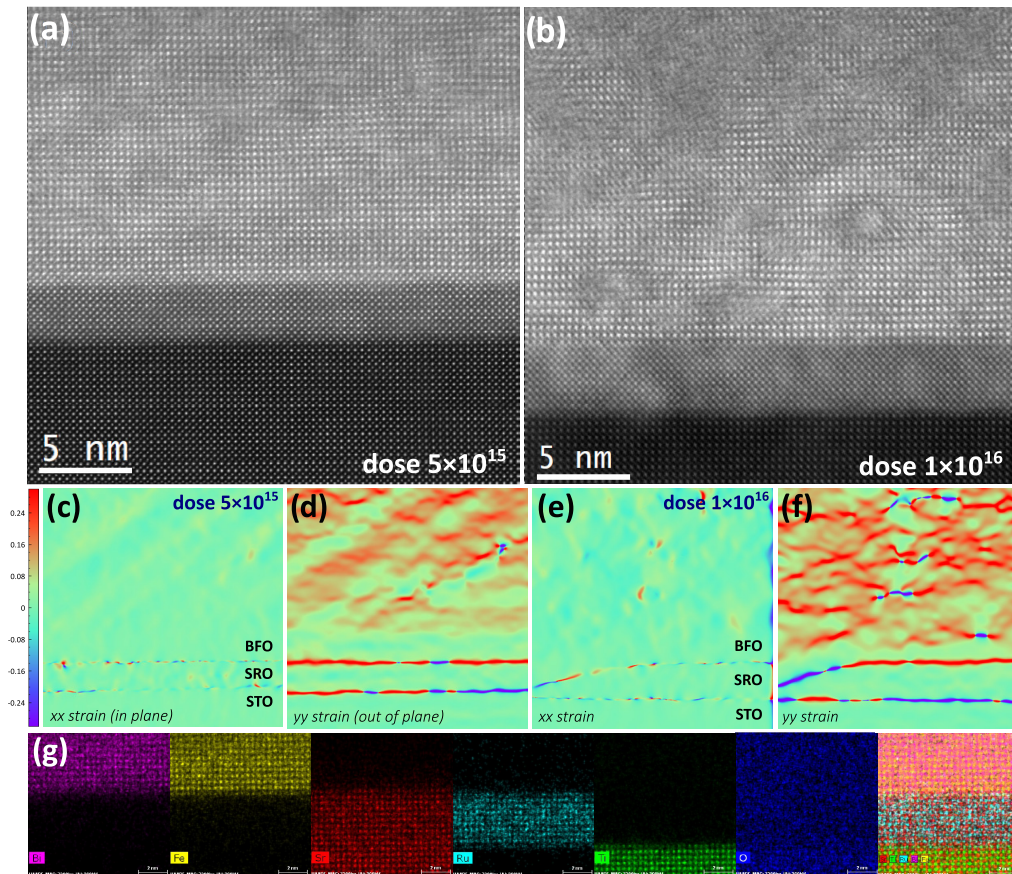


FIG. 3. [(a),(b)] STEM images (HAADF) of $\text{BiFeO}_3/\text{SrRuO}_3/\text{SrTiO}_3$ samples implanted with doses 5×10^{15} (a) and 1×10^{16} (b) He cm^{-2} . [(c)–(f)] GPA (geometrical phase analysis) of the strain in the epitaxial plane [(c),(e)] and out of plane [(d),(f)], using the SrTiO_3 substrate as a reference, of the samples with dose 5×10^{15} [(c),(d)] and 1×10^{16} [(e),(f)] He cm^{-2} . (g) EDX chemical analysis of the interface in the sample implanted with $5 \times 10^{15} \text{ He cm}^{-2}$.

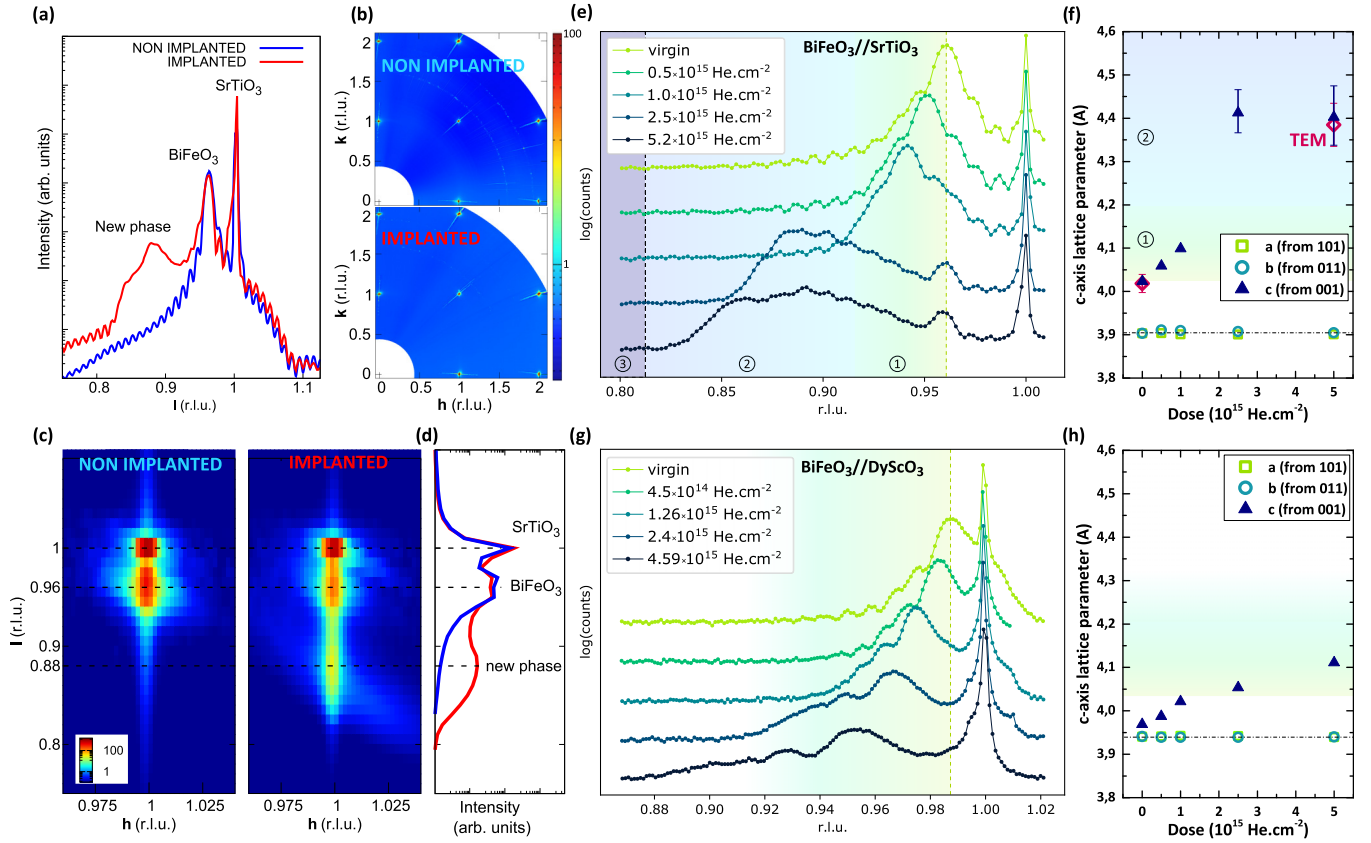


FIG. 4. X-ray diffraction results of nonimplanted and implanted (with a 5×10^{15} He cm $^{-2}$ dose) regions of a BiFeO $_3$ //SrTiO $_3$ thin film. (a) Specular reflectivity. (b) (h,k) reciprocal space maps integrated in the $-0.05 < l < 0.05$ range. (c) (h,l) reciprocal space maps measured at $k = 0.96$ and (d) the corresponding one-dimensional plot by integrating the intensity of the map contained in the $0.98 < h < 1.02$ range. (e) $\theta(2\theta)$ scans of regions implanted with various helium doses. (f) Extracted out-of-plane (blue triangles) and in-plane (green circles) lattice parameters (from 001, 101, and 011 Bragg peaks) as a function of the helium dose. The out-of-plane lattice parameters estimated from STEM observations are added as red diamonds. Similar experiments for a BiFeO $_3$ //DyScO $_3$ sample with (g) $\theta(2\theta)$ scans of regions implanted with various helium doses and (h) the extracted out-of-plane (blue triangles) and in-plane (green circles) lattice parameters (from 001, 101, and 011 Bragg peaks) as a function of the helium dose.

of the two structural phases, the pristine R-like phase and the new phase with enhanced tetragonality in the implanted region. Alternatively, the R-type signal could also arise from neighboring nonimplanted regions, partly probed due to the x-ray spot size that was slightly larger than the implanted region.

In order to study the conditions of appearance of this new phase under helium implantation, we performed implantations with increasing doses. The $\theta(2\theta)$ XRD scans, around the (001) Bragg peak of the SrTiO $_3$ substrate for doses ranging between 5×10^{14} and 5×10^{15} He cm $^{-2}$, are shown on Fig. 4(e). We observe the (001) peak of the BiFeO $_3$ layer progressively shifting towards higher c -axis lattice parameters with dose. Under 2.5×10^{15} He cm $^{-2}$ [region ①, in green Fig. 4(e)], the layer's (001) peak shifts continuously. At 2.5×10^{15} He cm $^{-2}$, however, we observe an abrupt change in the (001) Bragg signal of the layer [region ②, in blue Fig. 4(e)], with a strong shift of the layer peak that we interpret as the appearance of the new phase previously observed in Figs. 4(c) and 4(d) and the onset of the R-like to T-like BiFeO $_3$ structural transition. In this new phase (at 2.5×10^{15} He cm $^{-2}$ dose and above), we also observe the presence of a peak at the position of the (001)

peak of the virgin (nonimplanted) BiFeO $_3$ layer, as observed in Figs. 4(c) and 4(d). In this measurement, the spot size was well below the size of the implanted regions and its centering by means of (x, y) scans ruled out the possibility of signal coming from nonimplanted BiFeO $_3$. The presence of the (001) pristine-like BiFeO $_3$ peak therefore unambiguously points to a phase mixture in the implanted region.

The lattice parameters were extracted directly from the (001), (101), and (011) XRD peaks of the film in the different regions. They are shown as a function of the implanted helium dose in Fig. 4(f), the dotted line marking the lattice parameter of the SrTiO $_3$ cubic substrate. As observed previously, the in-plane lattice parameters are not modified under implantation.

To investigate the combined effect of epitaxial strain and implantation, we performed implantations with the same helium doses on a film synthesized on a DyScO $_3$ substrate, which has a lattice parameter closer to BiFeO $_3$ (-0.4% lattice misfit [35]). Figure 4(g) shows the $\theta(2\theta)$ XRD scans around the (001) Bragg peak of the DyScO $_3$ substrate for doses ranging between 5×10^{14} and 5×10^{15} He cm $^{-2}$. We see the (001) peak of the BiFeO $_3$ layer progressively shifting with dose, showing an increase of the out-of-plane lattice

parameter. Contrary to the results on the SrTiO_3 substrate, no abrupt modification is observed, and the c lattice parameter [reported in Fig. 4(h)] is in the same range than in the ① region of the Fig. 4(f) on the SrTiO_3 sample. This indicates a strained R-like structure with no phase transition. Like on SrTiO_3 , we observe no modification of the in-plane a and b lattice parameters, locked by the DyScO_3 lattice parameter [dotted line, Fig. 4(h)].

D. Discussion

By combining Raman spectroscopy, electron microscopy, and x-ray diffraction, we could access the structural changes due to implantation at different length scales, allowing for a more complete insight into the transition between the rhombohedral and supertetragonal phases of BiFeO_3 films than previously reported. Specifically, helium implantation is a way to observe the transition with a continuously varying parameter, as opposed to epitaxial strain that typically takes only a few discrete values fixed by the substrates.

Our TEM measurements, in particular, clearly show both the elongation of the unit cell and the partial amorphization. We indeed observe amorphized regions at $1 \times 10^{16} \text{ He cm}^{-2}$ dose, while at the same time, the c -axis lattice parameter extracted by Fourier transform from the nonamorphized regions presents a ratio with the a -axis lattice parameter which is close to the c/a ratio of the supertetragonal phase [30]. It therefore seems that despite the structural damage due to the loss of crystallinity of some regions, we continue to enhance the tetragonality of the still crystalline regions of the film towards the T phase. It is not possible to know if amorphization was also present in the previous study on He implantation of BiFeO_3 films using a large-scale ion implanter [23], as XRD is only sensitive to the crystalline regions. In our XRD data, where the dose was kept low enough to avoid amorphization, the elongation of the unit cell does not reach the c/a typical of the supertetragonal phase. Whether or not it is possible to fully transform into the supertetragonal phase on SrTiO_3 while remaining fully crystalline is still to be investigated.

The picture provided by our TEM and XRD data shows significant differences when compared to the same phase transition reported in Ref. [23] on $(\text{LaAlO}_3)_{0.3}(\text{Sr}_2\text{TaAlO}_6)_{0.7}$ (LSAT) and SrTiO_3 . We observe the transition towards a mixed phase with an enhanced tetragonality both at lower epitaxial strain and at lower doses: Herklotz *et al.* [23] observe a structural transition towards the T phase on LSAT, with a -2.6% lattice misfit and a $6 \times 10^{15} \text{ He cm}^{-2}$ dose, whereas we already see a similar behavior with enhanced tetragonality on SrTiO_3 where the lattice misfit is only -1.5% at a $2.5 \times 10^{15} \text{ He cm}^{-2}$ dose. These discrepancies are not negligible, and their origin is for the moment unclear. They could be due to an inaccurate estimation of the implanted dose or to a different local behavior, resulting in a strain gradient, which may be due to the difference in implantation technique. In particular, the presence of interfaces between implanted and nonimplanted regions, specific to the patterning possibilities of our implantation technique, can impact the strain relaxation mechanisms and account for a higher applied strain with respect to the dose as compared to large-scale implantation techniques. Moreover, the thickness and possible domain structure

differences can give rise to different stress field landscapes, which may account for the differences in our study. Furthermore, the energy of the accelerated He ions with the He-FIB we use is higher than with a large-scale ion implanter as used in Ref. [23]. Special attention should be paid to these aspects in future studies.

A noticeable difference also lies in the way the transition proceeds with increasing dose. In Ref. [23] the transition is described as appearing continuously under implantation with a progressive shift of the Bragg peak [cf. Fig. 1(b) of the Ref. [23] for the film grown on LSAT]. They further support the scenario of a continuously rotating polarization based on PFM and SHG observations. In our measurements, in contrast, the emergence of the T-like phase appears to be step-like with a visible phase coexistence, reminiscent of a first-order transition. We believe this is not, in fact, incompatible with their raw XRD data, where a splitting of the Bragg peak can be seen at intermediate doses. We hypothesize that the continuous character observed in PFM and SHG could result from an averaging effect that does not reflect the details of the local picture.

Finally, the comparison between Raman and XRD data sheds light on the disappearance of the Raman spectrum. We can see that the Raman signal disappears at a dose ($1 \times 10^{15} \text{ He cm}^{-1}$) where BiFeO_3 is still clearly in a slightly elongated R phase. Indeed, the $\theta(2\theta)$ XRD scan [Fig. 4(e)] still shows a narrow 001 Bragg peak, shifted from the pristine BiFeO_3 , but still showing no sign of transition from the rhombohedral-like structure. Therefore, the vanishing of the Raman signal cannot be attributed to the lower Raman intensity known for the T phase and cannot be understood as a signature of the transition towards the tetragonal-like structure. Instead, we suggest that it reflects a decrease of Raman susceptibility and polarizability due to the insertion of helium ions. This might be of importance also for the dielectric properties of the implanted films.

IV. CONCLUSION

Helium implantation has arisen recently as a powerful technique with the potential to modify and tune the strain state in a perovskite film. We have shown here, in particular, that local helium implantation by means of a helium ion microscope can enhance tetragonality in (001)-oriented BiFeO_3 thin films, increasing the out-of-plane lattice parameter up to 4% in films grown on DyScO_3 and up to 9% in films grown on SrTiO_3 , inducing locally a structural phase transition towards a mixed R-T phase.

Combined Raman spectroscopy, electron microscopy, and x-ray diffraction measurements allowed us to probe the structural changes both at the large scale and locally. Our local (TEM) study allowed us to determine the threshold dose for which amorphization starts to appear in implanted regions while observing elongations of the unit cell along the c axis up to values nearing the supertetragonal lattice distortion. Synchrotron XRD performed in the locally implanted regions allowed us to probe the onset of the transition between the rhombohedral-like structure and the supertetragonal phase. Our data suggest that this transition appears as a first-order transition, with an abrupt jump of the c -axis expansion at a

threshold dose (2.5×10^{15} He cm⁻¹ on SrTiO₃), which opens the discussion for understanding the underlying mechanisms at stake in this structural transition under implantation.

More generally, this work demonstrates the use of a helium microscope as a powerful mean for strain engineering by local helium implantation and opens technical possibilities for property tuning and patterning.

ACKNOWLEDGMENTS

This work was supported by the Fond National de la Recherche (FNR) of Luxembourg (PEARL CO-FERMAT, Project Code No. FNR/P12/4853155/Kreisel). We acknowl-

edge SOLEIL for provision of synchrotron radiation at the CRISTAL beamline (Proposal No. 20190831). TEM sample preparation and observation was carried out within the MAT-MECA consortium and supported by the Agence Nationale de la Recherche (ANR) under Contract No. ANR-10-EQPX-37. It has benefited from the facilities of the Laboratory MSSMat, CNRS, CentraleSupélec, Université Paris-Saclay, France. The author Inma Peral is supported by the Fond National de la Recherche (FNR) of Luxembourg (Grant No. FNR-Inter2015/LRSF). S.F. acknowledges financial support from a VENI grant (Grant No. 016.veni.179.053) of the Netherlands Organization for Scientific Research (NWO).

-
- [1] O. Bilani-Zeneli, A. D. Rata, A. Herklotz, O. Mieth, L. M. Eng, L. Schultz, M. D. Biegalski, H. M. Christen, and K. Dörr, *J. Appl. Phys.* **104**, 054108 (2008).
 - [2] K. Dörr, O. Bilani-Zeneli, A. Herklotz, A. D. Rata, K. Boldyreva, J.-W. Kim, M. C. Dekker, K. Nenkov, L. Schultz, and M. Reibold, *Eur. Phys. J. B* **71**, 361 (2009).
 - [3] A. Herklotz, J. D. Plumhof, A. Rastelli, O. G. Schmidt, L. Schultz, and K. Dörr, *J. Appl. Phys.* **108**, 094101 (2010).
 - [4] N. A. Pertsev, A. K. Tagantsev, and N. Setter, *Phys. Rev. B* **61**, R825 (2000).
 - [5] M. Tyunina, J. Narkilahti, M. Plekh, R. Oja, R. M. Nieminen, A. Dejneka, and V. Trepakov, *Phys. Rev. Lett.* **104**, 227601 (2010).
 - [6] B. G. Kim, *Solid State Commun.* **151**, 674 (2011).
 - [7] J. W. Guo, P. S. Wang, Y. Yuan, Q. He, J. L. Lu, T. Z. Chen, S. Z. Yang, Y. J. Wang, R. Erni, M. D. Rossell *et al.*, *Phys. Rev. B* **97**, 235135 (2018).
 - [8] J. H. Lee and K. M. Rabe, *Phys. Rev. Lett.* **104**, 207204 (2010).
 - [9] D. Sando, A. Agbelele, D. Rahmedov, J. Liu, P. Rovillain, C. Toulouse, I. C. Infante, A. P. Pyatakov, S. Fusil, E. Jacquet *et al.*, *Nat. Mater.* **12**, 641 (2013).
 - [10] A. Agbelele, D. Sando, C. Toulouse, C. Paillard, R. D. Johnson, R. Rüffer, A. F. Popkov, C. Carrétéro, P. Rovillain, J.-M. Le Breton *et al.*, *Adv. Mater.* **29**, 1602327 (2016).
 - [11] T. Yamada, T. Kiguchi, A. K. Tagantsev, H. Morioka, T. Iijima, H. Ohsumi, S. Kimura, M. Osada, N. Setter, and H. Funakubo, *Integr. Ferroelectr.* **115**, 57 (2010).
 - [12] J. Schwarzkopf, M. Schmidbauer, T. Remmele, A. Duk, A. Kwasniewski, S. B. Anooz, A. Devi, and R. Fornari, *J. Appl. Crystallogr.* **45**, 1015 (2012).
 - [13] A. J. Mao, H. Tian, X. Y. Kuang, J. W. Jia, and J. S. Chai, *RSC Adv.* **6**, 100526 (2016).
 - [14] M. C. Weber, M. Guennou, N. Dix, D. Pesquera, F. Sánchez, G. Herranz, J. Fontcuberta, L. López-Conesa, S. Estradé, F. Peiró, J. Iñiguez, and J. Kreisel, *Phys. Rev. B* **94**, 014118 (2016).
 - [15] S. Tinte, K. M. Rabe, and D. Vanderbilt, *Phys. Rev. B* **68**, 144105 (2003).
 - [16] Y. Liu, L. Ni, Z. Ren, G. Xu, C. Song, and G. Han, *J. Phys.: Condens. Matter* **21**, 275901 (2009).
 - [17] J. Wang, B. Wylie-van Eerd, T. Sluka, C. Sandu, M. Cantoni, X.-K. Wei, A. Kvasov, L. J. McGilly, P. Gemeiner, B. Dkhil *et al.*, *Nat. Mater.* **14**, 985 (2015).
 - [18] A. Kvasov, L. J. McGilly, J. Wang, Z. Shi, C. S. Sandu, T. Sluka, A. K. Tagantsev, and N. Setter, *Nat. Commun.* **7**, 12136 (2016).
 - [19] V. Sharma, A. Herklotz, T. Z. Ward, and F. A. Reboredo, *Sci. Rep.* **7**, 11166 (2017).
 - [20] H. Guo, S. Dong, P. D. Rack, J. D. Budai, C. Beekman, Z. Gai, W. Siemons, C. M. Gonzalez, R. Timilsina, A. T. Wong *et al.*, *Phys. Rev. Lett.* **114**, 256801 (2015).
 - [21] A. Herklotz, S. F. Rus, and T. Z. Ward, *Nano Lett.* **16**, 1782 (2016).
 - [22] A. Herklotz, A. T. Wong, T. Meyer, M. D. Biegalski, H. N. Lee, and T. Z. Ward, *Sci. Rep.* **6**, 26491 (2016).
 - [23] A. Herklotz, S. F. Rus, N. Balke, C. Rouleau, E.-J. Guo, A. Huon, S. K. C. R. Roth, X. Yang, C. Vaswani *et al.*, *Nano Letters* **19**, 1033 (2019).
 - [24] L. J. McGilly, C. S. Sandu, L. Feigl, D. Damjanovic, and N. Setter, *Adv. Funct. Mater.* **27**, 1605196 (2017).
 - [25] S. Saremi, R. Xu, F. I. Allen, J. Maher, J. C. Agar, R. Gao, P. Hosemann, and L. W. Martin, *Phys. Rev. Mater.* **2**, 084414 (2018).
 - [26] C. Zeiss, Microscopy Resolution Record Claimed by Carl Zeiss, <http://www.fabtech.org/news> (2008), http://www.fabtech.org/news/_a/microscopy_resolution_record_claimed_by_carl_zeiss/.
 - [27] C. D. Cress, D. Wickramaratne, M. R. Rosenberger, Z. Hennighausen, P. G. Callahan, S. W. LaGasse, N. Bernstein, O. M. van 't Erve, B. T. Jonker, S. B. Qadri *et al.*, *ACS Appl. Mater. Interfaces* **13**, 836 (2021).
 - [28] D. Lebeugle, D. Colson, A. Forget, and M. Viret, *Appl. Phys. Lett.* **91**, 022907 (2007).
 - [29] J. Wang, J. B. Neaton, H. Zheng, V. Nagarajan, S. B. Ogale, B. Liu, D. Viehland, V. Vaithyanathan, D. G. Schlom, U. V. Waghmare *et al.*, *Science* **299**, 1719 (2003).
 - [30] D. Sando, B. Xu, L. Bellaiche, and V. Nagarajan, *Appl. Phys. Rev.* **3**, 011106 (2016).
 - [31] D. Sando, A. Barthélémy, and M. Bibes, *J. Phys.: Condens. Matter* **26**, 473201 (2014).
 - [32] I. C. Infante, S. Lisenkov, B. Dupe, M. Bibes, S. Fusil, E. Jacquet, G. Geneste, S. Petit, A. Courtial, J. Juraszek, L. Bellaiche, A. Barthelemy, and B. Dkhil, *Phys. Rev. Lett.* **105**, 057601 (2010).
 - [33] S. Farokhipoor and B. Noheda, *Phys. Rev. Lett.* **107**, 127601 (2011).

- [34] S. Farokhipoor and B. Noheda, *J. Appl. Phys.* **112**, 052003 (2012).
- [35] A. Haykal, J. Fischer, W. Akhtar, J.-Y. Chauleau, D. Sando, A. Finco, F. Godel, Y. A. Birkhölzer, C. Carrétéro, N. Jaouen *et al.*, *Nat. Commun.* **11**, 1704 (2020).
- [36] C. J. M. Daumont, S. Farokhipoor, A. Ferri, J. C. Wojdeł, J. Íñiguez, B. J. Kooi, and B. Noheda, *Phys. Rev. B* **81**, 144115 (2010).
- [37] T. Wirtz, O. De Castro, J.-N. Audinot, and P. Philipp, *Annu. Rev. Anal. Chem.* **12**, 523 (2019).
- [38] R. Livengood, S. Tan, Y. Greenzweig, J. Notte, and S. McVey, *J. Vac. Sci. Technol. B* **27**, 3244 (2009).
- [39] S. Autier-Laurent, O. Plantevin, P. Lecoeur, B. Decamps, A. Gentils, C. Bachelet, O. Kaitasov, and G. Baldinozzi, *EPL (Europhys. Lett.)* **92**, 36005 (2010).
- [40] J. Wei, H. Ji, W. Guo, A. H. Nevidomskyy, and D. Natelson, *Nat. Nanotechnol.* **7**, 357 (2012).
- [41] J. F. Ziegler, *Nucl. Instrum. Methods Phys. Res., Sect. B* **219-220**, 1027 (2004).
- [42] J. A. Schneeloch, Z. Xu, J. Wen, P. M. Gehring, C. Stock, M. Matsuda, B. Winn, G. Gu, S. M. Shapiro, R. J. Birgeneau *et al.*, *Phys. Rev. B* **91**, 064301 (2015).
- [43] SrRuO₃ Crystal Structure - SpringerMaterials (2019), https://materials.springer.com/isp/crystallographic/docs/sd_1502783.
- [44] A. Schober, J. Fowlie, M. Guennou, M. C. Weber, H. Zhao, J. Íñiguez, M. Gibert, J.-M. Triscone, and J. Kreisel, *APL Mater.* **8**, 061102 (2020).
- [45] M. J. Hÿtch, E. Snoeck, and R. Kilaas, *Ultramicroscopy* **74**, 131 (1998).
- [46] H. Fukumura, H. Harima, K. Kisoda, M. Tamada, Y. Noguchi, and M. Miyayama, *J. Magn. Magn. Mater.* **310**, e367 (2007).
- [47] M. Cazayous, D. Malka, D. Lebeugle, and D. Colson, *Appl. Phys. Lett.* **91**, 071910 (2007).
- [48] M. N. Iliev, M. V. Abrashev, D. Mazumdar, V. Shelke, and A. Gupta, *Phys. Rev. B* **82**, 014107 (2010).